ARTICLE

OPEN

Vertically co-oriented two dimensional metal-organic frameworks for packaging enhanced supercapacitive performance

Ting Deng[1], Wei Zhang [1,2,3], Oier Arcelus[2], Dong Wang[1], Xiaoyuan Shi[1], Xiaoyu Zhang[1], Javier Carrasco[2], Teófilo Rojo[2] & Weitao Zheng[1]

Metal–organic frameworks (MOFs) are promising materials for batteries and super-capacitors. However, random crystal orientations and low conductivity can result in poor performance. Designing a convenient method to address these issues is therefore an important challenge. Here we describe an efficient strategy to fabricate self-supported MOF wall-like architectures with uniform orientation on carbon nanowalls (CNWs) as seedbeds. In addition, we gain molecular-level insight into the interface between CNWs and MOF nanosheets using density functional theory calculations. Our results suggest that assembled ions anchor on edge carbon atoms to match the matrix of the edges of CNWs, while the remaining ions self-assemble with terminal –COOH groups on p-benzenedicarboxylic acid ligands to form the structure. Our findings demonstrate a feasible method to fabricate integrated MOF electrodes with ideal orientations and, therefore, may pave the way to unlock the inherent high performance of MOF materials towards a number of engineering applications.

[1] State Key Laboratory of Automotive Simulation and Control and Department of Materials Science and International Center of Future Science and Electron Microscopy Center, Jilin University, Changchun 130012, China. [2] CIC Energigune, Albert Einstein 48, Miñano 01510, Spain. [3] Ikerbasque, Basque Foundation for Science, Bilbao 48013, Spain. Correspondence and requests for materials should be addressed to W.Z. (email: weizhang@jlu.edu.cn) or to J.C. (email: jcarrasco@cicenergigune.com) or to W.Z. (email: wtzheng@jlu.edu.cn)

Metal–organic frameworks (MOFs) are synthesized by joining metal-containing units with organic linkers to forge open crystalline framework. A variety of metal-containing units and organic linkers can be chosen for MOF preparation, which offer extensive flexibility[1–3] for tuning topologies, pore structures, sizes, and constituents[4] for a number of technological applications ranging from heterogeneous catalysis to electrochemical energy storage devices[5]. Besides being treated as templates[6] and precursors[7,8], MOFs can be directly utilized as active materials by incorporating redox metal centers into their structures, ascribed to their large specific area surface[9] and potential pseudo-capacitance sites[10,11]. This makes MOFs particularly interesting electrode materials for supercapacitors.

However, the low conductivity of MOFs hinders their straightforward application. Tremendous efforts towards solving this issue have resulted in the design of improved MOFs, such as metal-ion based MOFs[12–16] and other composite materials[17]. In spite of such success stories, on typical substrates MOF crystals grow in random orientations, which strongly reduces specific areas, limits the effective permeation of electrolytes to electrochemical surfaces, and lowers the overall utilization of the MOF active sites. For instance, in porous MOFs local pores are sealed, triggering dead volumes, whereas in planar MOFs some planar surfaces are mutually covered causing the shrinkage of gap spacing. These scenarios have become a bottleneck for unlocking the full potential performance of MOFs[18].

There are many methods to control MOF growth[19–22], but to date the most effective way to synthesize highly oriented materials and control their morphologies involves using templates able to govern nucleation and growth processes. Very recently, an oriented MOF has been synthesized on Cu(OH)$_2$, showing improved optical performance[23]. Unfortunately, in the case of electrochemical energy storage applications, the overall performance of the material is strongly affected by conductivity. If the template is not properly removed, it may degrade electrochemical performance. Even if substrate removal is successful, it may unavoidably trigger MOF deformation or even destruction after calcination or etching by polar solvents[24]. Hence, typical templating methods are probably not the best way to synthesize self-supported MOFs with controlled orientation. Methods to precisely locate MOFs on substrates for a wide range of applications have been reviewed[25,26]. However, for electrochemical energy storage systems, like supercapacitors, there are no efficient methods. Specifically, for batteries and supercapacitors, relatively large templates with homogeneous loadings of controlled MOFs require a more convenient fabrication protocol.

For these applications, we propose an easy strategy to prepare a binder-free, self-supported, and highly oriented MOF electrode using a substrate coated with carbon materials to match the initial MOFs and shape the further growth[27,28]. Herein, we demonstrate that the growth of highly vertically oriented MOF nanosheets (VMSs) is successfully shaped by plasma enhanced chemical vapor deposition (PECVD)-prepared carbon nanowalls (CNWs) on Ni foam. We also synthesize a Ni MOF sample without CNWs in a control experiment. We further exploit this VMS/CNW/Ni foam as an integrated supercapacitor electrode and show how this binder-free MOF electrode exhibits improved performance compared to the control sample.

Results

Structural characterization of the vertical Ni MOF.
Compared to traditional porous materials, the most appealing advantage of MOFs is that using different metal ions and organic linkers so that MOFs can be finely designed to exhibit one-, two-, and three-dimensional (1D, 2D, and 3D) MOF structures[4,26]. Here we used

p-benzenedicarboxylic acid (PTA) as the ligand and nickel nitrate as ion source to synthesize a layered 2D MOF through a reported method with modifications[10]. X-ray diffraction (XRD) data of the synthesized Ni MOF is provided in Fig. 1a, which is in accordance with the simulated curve (CCDC 638866) indicating that the MOF we synthesized belongs to MOF-24, a layered MOF. The lattice parameters a, b, and c are 10.2077, 8.0135, and 6.3337 Å, respectively. However, it shows relatively low crystallinity because of a short reaction time (6 h). Judged from the X-ray absorption fine structure (XAFS) spectrum in Supplementary Figure 1, the absorption K-edge for the synthesized MOF shows no difference with NiO, suggesting that Ni valence state is +2[29]. Scanning electron microscopy (SEM) images (Fig. 1b) reveal that the Ni MOF is made up of flakes with irregular sizes ranging from nano- to micrometer scale. The elongated reaction time (12 h) leads to a higher crystallinity and a well-defined layered structure (Supplementary Figure 2) as confirmed by transmission electron microscopy (TEM) analysis in Supplementary Figure 3. Isothermal N_2 adsorption–desorption analysis (Supplementary Figure 4) was performed to further evaluate the porous features of the synthesized MOF. The isotherm is a typical IV type curve. Mesoporous structure was indicated by the loop in the nitrogen adsorption isotherm (the inset of Supplementary Figure 4), and the specific surface area is 32.72 m^2 g^{-1} calculated by Brunauer–Emmett–Teller (BET) method, which is probably due to the random layered structure and its relatively low crystallinity. The synthesized MOF with random orientations would still shuffle on the current collector when fabricated into an electrode, which may have a negative effect on electrochemical behaviors together with low conductivity. As mentioned above, even though MOFs show a promising future in energy storage and the layered structure is favorable for electrochemical properties, this orientation chaos would limit permeation of electrolyte and thus lower effective redox sites and the utilization of active materials. In addition, the electrochemical performance is expected to be further hindered by the poor crystallinity and low BET surface area associated to the short reaction time. In particular, using the synthesized Ni MOF pressed onto a nickel foam as a capacitor electrode, we found an electrochemical performance of 684 F g^{-1} at the current density of 1 A g^{-1} (Supplementary Figure 5). However, when the electrode is discharged at a higher current density of 16 A g^{-1}, the capacitance can only reach 249 F g^{-1}, which clearly indicates poor rate capability. In addition, one can see impurity peaks in the XRD pattern, which we believe is due to the short reaction time. To prove that, we have elongated the reaction time to 12 h and the XRD pattern has shown better crystallinity and no impurity peaks were observed (Supplementary Figure 6a). The corresponding electrochemical performance has also been improved (Supplementary Figure 6b and c), and the capacitance can reach 793, 711, 568, 444, 355, and 213 F g^{-1} at the current density of 1, 2, 4, 8, 16, and 32 A g^{-1}, respectively. However, the overall performance is still less desirable. This highlights the need for suppressing MOF random orientation in order to achieve improved maximum capacitances and capacitance retentions, especially at high current densities.

Recently, it has been reported that combining precursors of MOFs and other hybrid materials, like graphene, in the synthesis process can change MOF morphology[27,28,30]. In particular, tuning the content of doping species in the precursors can lead to a range of morphologies, such as polyhedrons, layered structures, or even nanowires. It is assumed that doped precursors induce lattice distortions of MOFs. However, the layered structure of Ni MOF is favorable for supercapacitive properties which need to be preserved. Herein, we designed a novel and feasible approach to synthesize a vertically oriented MOF without changing its layered structure and where the
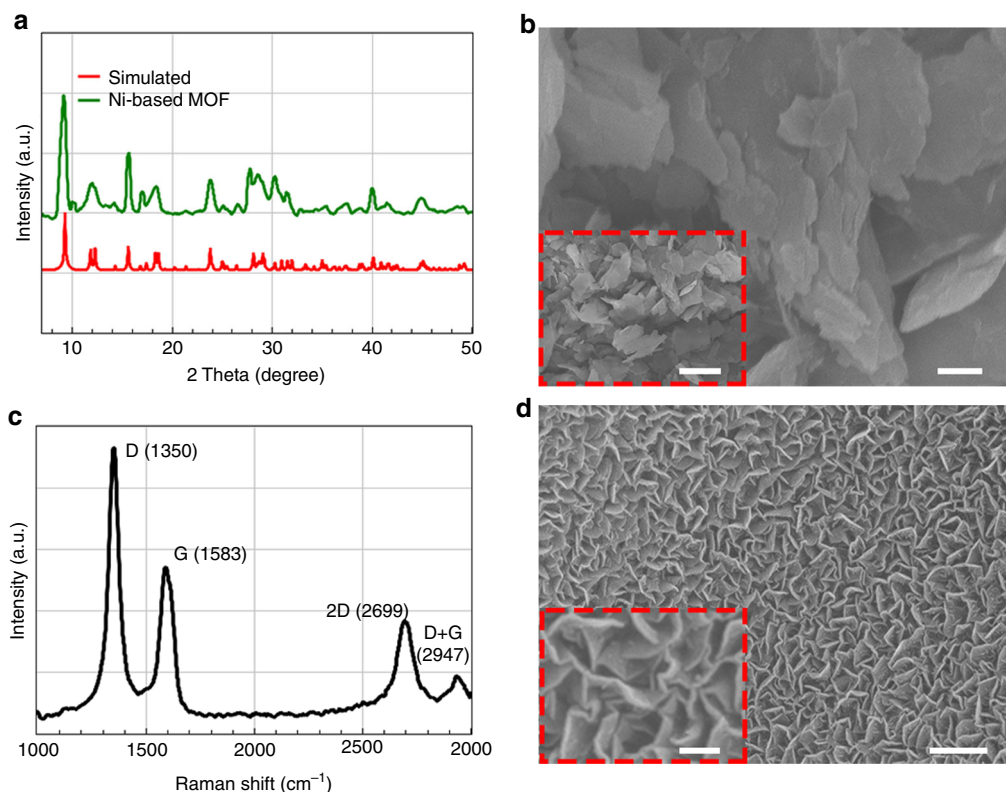
Fig. 1 Characterization of Ni MOF powders and carbon nanowalls. **a** XRD characterization of MOF powders. **b** SEM images of Ni MOF show flake-shape and random orientations. Scale bar = 400 nm. Inset: a lower magnification showing random orientations of MOF flakes. Scale bar = 1 μm. **c** Raman spectrum of PECVD prepared carbon nanowalls. **d** SEM images of PECVD prepared carbon nanowalls with different magnifications. Scale bar = 500 nm. Inset: a higher magnification. Scale bar = 50 nm

removal of CNWs is unnecessary. On the other hand, the existence of CNWs will facilitate the electron transfer as well. In principle, uniform oriented dopants are a good seedbed for uniformly growing oriented MOF without modifying the structure, since these templates only affect adjacent precursors, match the matrix of initial MOFs, and do not induce lattice distortions during further MOF growth. So, we utilize carbon nanowalls as the seedbed and the edges of CNWs as the molding for oriented MOF synthesis, which is also highly conductive and, therefore, needs no removal.

CNWs can grow vertically oriented on Ni substrates prepared by PECVD[31–33]. This technique is particularly well suited due to its feasibility and potentiality for large-area production with reasonable growth rates. In this work, we grew CNWs on the substrate without any seed catalyst. When the Ni foam was heated up to 800 °C in the mixture of CH_4 and Ar, vertically oriented CNW coating was produced on the Ni foam after 30 min of growth. The Raman spectrum for CNWs is in Fig. 1c showing four prominent peaks at 1350 cm^{-1}, 1583 cm^{-1}, 1620 cm^{-1}, and 2699 cm^{-1}, which correspond to D, G, 2D, and D+G band, respectively. For a qualitative analysis of CNWs, we measured the intensity ratio between the D band (I_D), which corresponds to the induced disorder, and the G band (I_G), which corresponds to the intrinsic feature of sp^2 carbon. The I_D/I_G value is 1.67, which means a relatively high degree of structural disorder and crystal defects for the CNWs. Furthermore, I_{2D}/I_G is ~0.69, which further confirms the multi-layered structure of the prepared CNWs. Figure 1d shows a typical top-view SEM image. The reticulate walls of carbon materials were formed with the average side length of unit wall of approximately 200–400 nm and the thickness of about 20–30 nm. During the PECVD fabrication,

pristine graphitic islands were formed on the Ni foam with a planar growth until impingement with other islands. Then, the newly formed grain boundaries on the edges of basal islands pushed the sp^2 bonds upward. Free carbon out of CH_4 in the plasma continuously provided atoms to the growing hexagonal lattice. The relevant defects mainly exist at the edges of CNWs, which are, in principle, favorable nucleation sites for the growth of MOFs.

During the synthesis of Ni MOF, we use CNWs as seedbeds for MOF anchoring and constructing so that we put the CNWs in the mixture of MOF precursors. After the synthesis, VMSs were coated on the CNW substrate (Fig. 2a, b & c). The MOF layers are vertically, separately, and finely dispersed on CNWs without any agglomeration present in Ni MOF, showing a morphology and orientation very similar to that of CNWs (the inset of Fig. 2a). Figure 2b shows that these MOF sheets are mutually inter-connected to form the vertical structure. And to further confirm this vertical 2D MOF network, the electrode on SEM sample stage was examined from different angles of view (the inset of Fig. 2b). One can identify that the 2D MOF is vertically oriented on carbon CNWs. However, a high-magnification SEM image (Fig. 2c and inset) reveals that CNWs lie beneath these VMSs, and vertical and reticulate MOF flakes with bigger sizes grew indeed upon the CNWs. The layered feature of the oriented MOF was also confirmed (Supplementary Figure 7), which is the same as previously prepared MOF with random orientations. To confirm the vertical structure, we have taken SEM images of the edge of Ni foam (Supplementary Figure 8). In Supplementary Figure 8 one can clearly see that Ni foam was well coated by CNWs, upon which MOF sheets are vertically oriented. As mentioned above, defects on the edges of CNWs may provide
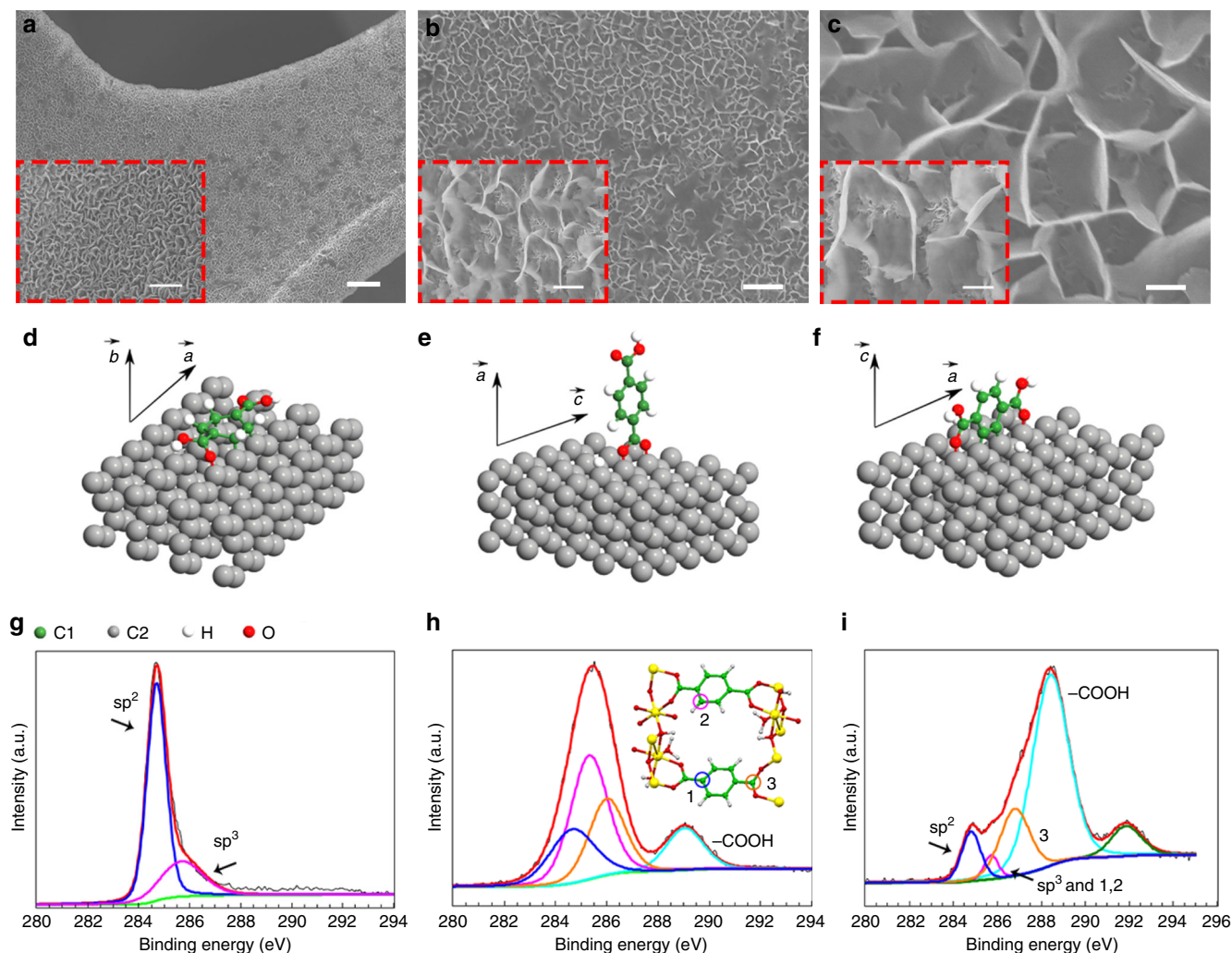
Fig. 2 Characterization of VMS/CNW and its interfaces along with DFT investigations of growth mechanism. **a**-**c** SEM images of vertically oriented MOF nanosheets on CNWs with an increasing magnification. Scale bars = 10 μm, 4 μm, and 400 nm, respectively. The inset of (**a**) is the SEM image of CNW and the insets of (**b**) and (**c**) are SEM images of VMS/CNW with higher magnification. Scale bars = 800 nm, 1 μm, and 500 nm, respectively. **d**-**f** DFT-optimized structures of the most stable configurations found, for each PTA adsorption mode planar (**d**), vertical (**e**), and side (**f**). Vectors on each figure represent the preferred growth directions of the Ni MOF, given each type of PTA absorption mode as its constituent building blocks. Red and white balls stand for O and H atoms, respectively. Carbon atoms of the PTA molecule (graphite) are green (gray). **g**-**i** XPS spectra for CNWs, Ni MOF, and VMS/CNW interface; the inset of (**h**) is the coordination environment of Ni MOF and the yellow balls are for Ni atoms

nucleation sites for VMS growth and, therefore, we speculate that PTA molecules and Ni^{2+} are initially anchored on the edge of graphitic surfaces where nascent MOFs were yielded. Then, with the stiffness of the organic linkers provided by the benzene ring of PTA molecules, the epitaxial growth of the rest of metal ions and organic linkers occurred along vertically oriented graphitic planes, resulting in uniform oriented VMSs.

Investigation of VMS growth mechanism. In order to gain molecular insight into this, we investigated the anchoring mechanism of PTA on the edge (prismatic) surface of graphite using density functional theory (DFT) calculations. To this end, we considered a range of possible adsorption sites, adsorption mechanisms (molecular and dissociative), and molecule orientations (see Supplementary Figures 9 to 12) because how PTA molecules are adsorbed on CNW influences the growth of VMS. Table 1 summarizes the adsorption energies of the three most stable structures for the three main PTA configurations: planar, vertical, and side orientations. In Fig. 2d, e & f we show the most

stable adsorption geometries for each of these three orientations. Owing to the highly reactive nature of the dangling bonds of C atoms in the edge surface of graphite, all computed adsorption energies correspond to strongly exothermic processes with respect to PTA in gas phase. Overall, we found that PTA molecules prefer to adsorb in a side orientation on top of graphitic ridges, giving rise to the cleavage of two C-H bonds, with an adsorption energy of −17.1 eV. Notice that the two dissociated H atoms are co-adsorbed on nearby C atoms. Adsorption in a planar orientation is 3.4 eV less favorable than side-oriented adsorption, whereas vertical-oriented molecules are 8.9 eV less stable. This result suggests that MOF upward growth on top of edge surfaces is enhanced along the c-axis, whereas growth along a- and b-axes will be much less preferred. This is fully consistent with the observed VMS growth on CNWs and provides molecular-level support to our experimental findings. To get more visual information, we conducted scanning transmission electron microscopy (STEM) and energy-dispersive X-ray (EDX) analysis (Supplementary Figure 13). The Pt layer was used to protect the MOF

structure from the high energy electron beam. In the red square of STEM image is a VMS structure. In the VMS, we can see that Ni and O also appear on the edges of CNWs, which is in accordance of the proposed growth mechanism and DFT calculations that PTA and Ni ion anchor on the edges of CNWs to form the initial MOFs that match the matrix of edges of CNWs.

Metal ions and linkers can then continually self-assemble with terminal –COOH groups on PTA to stabilize the whole architecture, forming a well-oriented MOF structure.

To get further experimental knowledge of the connection between CNWs and VMSs, we used X-ray photoelectron spectroscopy (XPS) to investigate the CNW/VMS interface. The XPS spectrum for the CWNs (Fig. 2g) can be decomposed into two components, corresponding to carbon atoms in sp^2- and sp^3-hybridized carbon at 284.5 and 285.7 eV, respectively. The XPS spectrum (Fig. 2h) for Ni MOF powders also shows two main components. The inset in Fig. 2h corresponds to the coordination environment of Ni MOF, showing three kinds of carbon atoms labeled as 1, 2, and 3 which are well decomposed in the main peak. Accordingly, the area ratio of these three kinds of carbon atoms is 1:1.9:1.1, which is in accordance with the inset mode of Ni MOF. In addition, the peak at 289 eV belongs to –COOH at edges of the Ni MOF structure. As in the interface between CNWs and MOF (Fig. 2i), the peak intensity of –COOH is very strong indicating that many –COOH species are adsorbed on edges of CNWs, which agrees well with the DFT results. In

Table 1 Adsorption energies computed with DFT of the three most stable configurations for each mode (planar, vertical, and side)

$E_{PTA@C-planar}$ (eV)	$E_{PTA@C-vertical}$ (eV)	$E_{PTA@C-side}$ (eV)
−13.7	−8.2*	−17.1†
−9.3†	−6.6*	−16.9†
−7.7*	−6.4*	−15.4¶

The *, †, and ¶ represent that one, two, or four hydrogen atoms dissociated from the PTA molecules, respectively
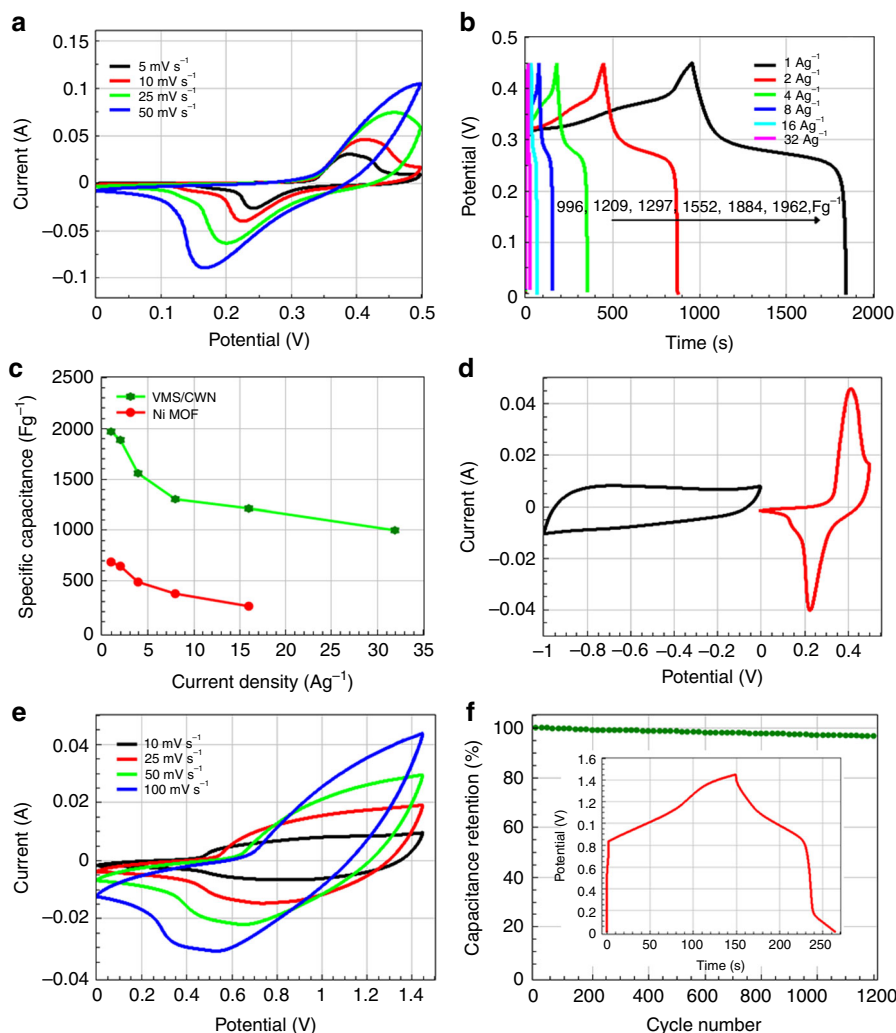

Fig. 3 Electrochemical characterizations of VMSs/CNWs/Ni foam electrode and corresponding VMS-active carbon asymmetric capacitor. **a** Cycle voltammetry curves with different scan speeds (vs. SCE). **b** Galvanostatic charge/discharge curves at different current densities, the highest specific capacitance reached 1962 F g^{-1} at a current density of 1 A g^{-1} (vs. SCE). **c** Specific capacitances at different current densities of Ni MOF powders and VMS (vs. SCE). **d** Cycle voltammetry curves of activated carbon (black) and VMSs/CNWs/Ni foam (red) electrodes at 10 mV s^{-1} (vs. SCE). **e** Cycle voltammetry curves of the asymmetric capacitor collected at different scan speed (vs. SCE). **f** The cyclability of the capacitor, it can hold 97% of its initial capacitance after 1200 cycles. The inset is galvanostatic charge/discharge curve at 0.5 A g^{-1} (vs. SCE)

**Table 2 MOF performances in the application of supercapacitors**

Materials	C_M (F g^{-1})	$C_{(MCD\ or\ MSR)}$ (F g^{-1})	Refs.
437-MOF	150	56 (8 A g^{-1})	16
Ni MOF	1127	668 (10 A g^{-1})	10
Zn-doped Ni MOF	1620	854 (10 A g^{-1})	11
UIO-66	1144	369 (50 mV s^{-1})	15
Cu-LCP	1274	568 (20 A g^{-1})	14
Co-LMOF	2474	1024 (20 A g^{-1})	12
Pillared Ni MOF	552	438 (20 A g^{-1})	13
Ni-MOFs@GO	2192	1024 (20 A g^{-1})	17
VMS/CNW	1962	996 (32 A g^{-1})	This work

C_M and $C_{(MCD\ or\ MSR)}$ stand for the maximum specific capacitance and the specific capacitance calculated at the maximum current or scan rate

addition, there is another peak at 291.8 eV that probably belongs to -C-[O-Ni]$_n$ bonds indicating that besides the physical adsorption, chemical bonding also took place to help MOF anchoring on CNWs. The Raman spectrum for VMSs/CNW is shown in Supplementary Figure 14. The I_D/I_G value is reduced to 1.42, whereas the I_{2D}/I_G value increased to 0.87 due to the fact that Ni MOF nanosheets with fewer layers growing on CNWs reduced the overall structural disorder and crystal defects.

Overall, the proposed growth mechanism can be separated into two steps which is shown in Supplementary Figure 15. First, linker PTA molecules adsorb in a side orientation on top of carbon atoms at edges, and the nascent MOFs are self-assembled in a side orientation to match the matrix of CNW edges. Then, additional metal ions and linkers continually and vertically self-assemble with terminal −COOH groups on PTA to stabilize the whole architecture, forming a well-oriented MOF structure. As one can see, some MOF sheets incline on CNWs at some regions, which is probably because that the edges of graphitic planes on CNWs are curved for MOF growth. As the reaction time was extended, random and large MOF sheets show up instead of the vertical orientation (Supplementary Figure 16), and these MOF sheets agglomerated that damaged the architecture and fell off the CNWs.

Electrochemical performance evaluation. We use VMS/CNW/Ni foam as an integrated supercapacitor electrode in 1 M KOH. Figure 3 shows the electrochemical performance of VMSs. There is a pair of redox peaks (Fig. 3a) that corresponds to mutual conversion of Ni^{2+} and Ni^{3+} species, which is companied with intercalation/de-intercalation of OH$^-$. This process can be represented by the following equations[10,34]:

$$Ni(II)_s + OH^- \leftrightarrow Ni(II)(OH)_{ad} + e^- \qquad (1)$$

$$Ni(II)(OH)_{ad} \leftrightarrow Ni(III)(OH)_{ad} + e^- \qquad (2)$$
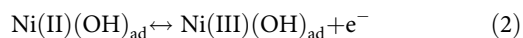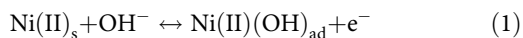
Two charge/discharge platforms imply the Faradaic behavior of VMSs and the best specific capacitance can reach as high as 1962 F g^{-1} at a current density of 1 A g^{-1} (Fig. 3b), which can be calculated according to the equation: $C_m = C/m = (I \times \Delta t)/(\Delta V \times m)$, where C_m (F g^{-1}) is the specific capacitance, I (mA) the discharge current, Δt (s) the discharging time, ΔV (V) represents the potential drop during discharge process, and m (mg) the mass of MOF. At higher current densities, VMSs show high capacitances (1884, 1552, 1297, and 1209 F g^{-1} at 2, 4, 8, and

16 A g^{-1}, respectively). Even at a current density of 32 A g^{-1}, the capacitance still reached 996 F g^{-1} (51% of its best), which indicates that VMSs have an excellent rate capability (Fig. 3c) compared to Ni MOF by no virtue of the uniformly upright orientation. To the best of our knowledge, 996 F g^{-1} at 32 A g^{-1} is the highest for a MOF material reported to date. Electrochemical impedance spectroscopy was also utilized to characterize VMSs/CNWs/Ni foam and Ni MOF electrodes, respectively (Supplementary Figure 17). The inset is the electrical equivalent circuit used for fitting impedance spectrum. R_s represents a combined resistance of ionic resistance of electrolyte, intrinsic resistance of substrate, and contact resistance at the active material/current collector interface. R_{ct} corresponds to the charge-transfer resistance (the semicircle in the high-frequency range). CPE is the constant phase element and W is the Warburg impedance. The Ni MOF with random orientation was pressed onto Ni foam, the calculated resistance is 3.2 Ω, which is due to poorly conductive nature of MOF. However, after the growth of MOFs on CNW, the resistance is reduced to 2.6 Ω, which is attributed to high conductivity of CNW and the resultant highly uniform orientation of MOFs. Accordingly, an asymmetric VMS-active carbon capacitor was fabricated (Fig. 3d) with 1 M KOH solution as the electrolyte. Figure 3e shows the cycle voltammetry curves with different scan speeds ranging from 10 to 100 mV s^{-1}. There is no obvious change for the curves, which indicates the good rate capability of this capacitor. The energy density of the asymmetric capacitor is 10 Wh kg^{-1} at a power density of 1450 W kg^{-1}. The cycling performance of the capacitor is also very stable, with 97% of its initial capacitance after 1200 cycles. To confirm the stability of the structure after the stability test, we also conducted Fourier transform infrared (FT-IR) experiment (Supplementary Figure 18). The FT-IR spectra of the as-prepared VMSs and the ones after 1200 times of charge/discharge cycles show quiet similar shapes. Both spectra present characteristic bands of the carboxylate within 1400–1650 cm^{-1} as well as the vibrations of O-Ni-O groups at 500–900 cm^{-1}. The wide band around 3400 cm^{-1} is assigned to the O-H stretching modes of interlayer water or methanol and of H-bound OH group, whose relative intensity compared to that of the characteristic band of carboxylate was enhanced after reacting with KOH electrolyte. After 1200 times of charge/discharge cycles, a sharp and intense band appeared at 3647 cm^{-1}, which is characteristic of free OH groups because of OH$^-$ ions penetrated into the electrode. The similar shapes of both FT-IR spectra indicate the robustness of the vertically aligned structure, which is in accordance with the stability test. This enhanced performance of the electrode and its corresponding capacitor have demonstrated that the uniform vertically orientated structure prevents MOF agglomeration, endows MOF with superior supercapacitive properties, and unlocks the promising future of MOFs with multiple virtues to be electrochemical-active materials.

The highly uniform orientation of the MOF not only facilitates electrolyte permeation, but also provides the shortest ion pathways for ion intercalation and de-intercalation. The CNWs beneath VMS provided facile electron transport because of intrinsically high electrical conductivity, which lead to good rate ability of the MOF. Table 2 summarizes the performance of MOF-based supercapacitors recently proposed in the literature. We see that our strategy harvests a considerable specific capacitance and promote the rate capability of the MOF at the same time; even at a 32 times larger current, the capacitance retention is 51%. It is also important to point out that the conductivity of MOFs is usually poor[35,36], and agglomeration of MOFs would further hamper the full use of potential active sites

and degrade the performance. Our strategy triggers nanocrystallization, which not only shorten the ion diffusion path, but also expand the specific area and increase active sites. Together with the vertical structure, nanocrystallization can increase effectively the electrochemical-active surface, enhancing the utilization ratio of redox sites and yielding the high specific capacitance. In addition, the nanocrystallization prevents the MOF from agglomeration and increases the electrode/electrolyte contact area[37,38]. Additionally, the intimate connection of CNWs and VMSs avoids binders, which play a vital role in traditional electrode fabrication process and can greatly affect electrode performance. We see therefore that the direct growth of VMSs on CNWs not only excludes the potential influences of binders, but also improves the electrochemical behaviors and provides a new highly efficient strategy to synthesize uniformly oriented MOF architecture that can upgrade performance for a wide range of applications.

Here we demonstrated that vertically oriented 2D layered MOF nanosheets grew directly on CNW and are a promising integrated electrode. However, many important issues remain in order to consistently prepare oriented MOFs with a variety of dimensions and morphologies. We put forward that by controlling the synthesis conditions, matrixes, or seedbeds in precursors, one should be able to shape MOF growth in selected directions. Such orientation control can therefore boost the performance of MOFs not only for energy storage application, but also in sensing, catalysis, and other applications.

Discussion

In summary, vertically oriented MOF nanosheets were synthesized by using CNWs which are utilized as seedbeds for MOF growth. PTA molecules adsorb in a side orientation on top of carbon atoms at edges, and the nascent MOFs are self-assembled in a side orientation to match the matrix of CNW edges, while the remaining ions self-assemble with a side orientation to forge the VMS structure on top of graphitic ridges. We also tested this integrated MOF electrode as binder-free supercapacitor electrode, exhibiting promising properties. The observed high performance is attributed to the well-defined orientation of the MOF nanosheets, which enhances the utilization of active sites for redox reactions and shortens ion diffusion paths. In addition, nanocrystallized compositing with CNWs facilitates electron transfer. Therefore, our vertically oriented MOF successfully demonstrates that uniform orientation can improve MOF performance in practical applications. This strategy may also open up new opportunities for controlling MOF growth and patterning to pursue superior properties in a wide range of applications.

Methods

Synthesis of Ni MOF powder. The Ni MOF was synthesized through a reported method with some modifications. Typically, 1 mmol of PTA (≥ 99%, Sinopharm Chemical Reagent Co., Ltd) and 1.5 mmol of nickel nitrate hexahydrate (Ni (NO₃)₂·6H₂O, AR, ≥ 98.0%, Sinopharm Chemical Reagent Co., Ltd) were dissolved in 20 ml N,N-dimethylformamide (DMF, ≥ 99.5%, Sinopharm Chemical Reagent Co., Ltd) in a vial with a capacity of 50 ml. After stirring at room temperature for 30 min, the vial was kept at 120 °C for 6 h. After cooling to room temperature, the green product was washed with DMF three times. Then, the precipitates were dried at 60 °C overnight, and herein Ni MOF was obtained.

Synthesis of carbon nanowalls. CNWs were synthesized on Ni foam (1 cm² in area) by PECVD. Before being put into the vacuum chamber, the Ni foam was ultrasonically cleaned with acetone, hydrochloric acid, and distilled water for 10 min, respectively. After the vacuum of the PECVD chamber was down to 10 Pa, a pressure of 200 Pa by introducing Ar gas (20 sccm) was kept until the Ni foam was heated to 800 °C. Then, the flow rate of Ar was changed to 80 sccm, and CH₄ (20 sccm) was introduced into the chamber. During the deposition, the plasma power was kept at 200 W. After 30 min of deposition, the whole system was naturally cooled down to ambient temperature under Ar atmosphere.

Synthesis of vertically oriented MOF/CNW composite. The CNWs/Ni foam was placed into the mixture of precursors for the synthesis of the Ni MOF. Then, the vial was kept at 120 °C for 6 and 12 h, respectively. After cooling to room temperature, the Ni foam was washed with DMF for several times and transferred to an oven at 60 °C overnight. Then, the vertically oriented MOF nanosheets/carbon nanowalls/Ni foam (VMS/CNW/Ni foam) electrode was obtained.

Physical characterization. Surface morphology of the Ni MOF, carbon nanowalls, and VMS/CNW/Ni foam electrode was studied by using SEM (Hitachi SU8000 scanning electron microscope). The detailed microstructural characterization was performed by TEM (JEOL JEM-2100F). A cross-section lamella of VMS/CNW/Ni foam prepared by using focused ion beam was used for STEM image and corresponding EDX analysis by Themis Z (FEI), operated at 200 kV. The XRD measurement was operated by a RIGAKU D/MAX 2500 instrument (λ = 1.54 nm). Raman spectroscopy was performed with a 514.5 nm Ar⁺ laser excitation (T64000 Horiba, a laser power of 7 mW). XPS was carried out by a ESCALAB-250 instrument with a monochromatic Al Kα radiation source and a hemisphere detector with an energy resolution of 0.1 eV. FT-IR spectra were obtained from Perkin Elmer Spectrum One B instrument. XAFS were collected at Beijing Synchrotron Facility (BSRF) on beamline 1W1B. The BSRF storage ring is operated at the electron energy of 2.2 GeV with beam current of 250 mA. A Si (111) double-crystal monochromator was applied. The beam size used at the sample position was 900 × 300 μm².

Electrochemical characterization. Electrochemical measurements were carried out on a computer-controlled potentiostat (CHI660E, CH Instrument, Shanghai) with a three-electrode electrochemical cell containing 1 M KOH aqueous solution as electrolyte. The working electrode was the VMS/CWN/Ni foam. A platinum plate and an SCE were used as counter electrode and reference electrode, respectively. The electrolyte (1 M KOH) was prepared from high purity KOH pellets (AR, ≥ 85.0%, Sinopharm Chemical Reagent Co., Ltd) by adding 56 g of pellets to 1 L distilled water. The Ni MOF and active carbon (AC) electrodes were fabricated using a same method as follows: a mixture of Ni MOF or AC, acetylene black, nafion (wt%: 85:10:5), and a small amount of ethanol was prepared by stirring 6 h to produce a homogeneous paste. This paste was pressed onto Ni foam (1 cm² in area) to produce Ni MOF or AC electrode. A two-electrode configuration was used to measure the performance of an asymmetric supercapacitor in 1 M KOH aqueous electrolyte solution. The working electrodes were the prepared VMS/CNW/Ni foam and AC electrodes mentioned above, and they were placed together and separated by a porous non-woven cloth separator. The mass loading of AC is about 5 mg, while the mass of VMSs ranges from 1 to 1.5 mg. Then, cyclic voltammetry was used to investigate its activity. Its charge/discharge ability was measured by a galvanostatic test. The energy and power densities of the asymmetric capacitor were calculated as follow: $E = 0.5 \times C \times V^2$, $P = I \times V \, m^{-1}$, where E (Wh kg⁻¹) is the energy density and P (W kg⁻¹) is the power density.

Computational details. DFT calculations were performed using the Vienna Ab-initio Simulation Package 5.4.1 code[39–41]. We used the semilocal Perdew–Burke–Ernzerhof (PBE)[42] exchange functional in combination with the latest generation of Grimme's dispersion-corrected approach (D3)[43] with the Becke–Johnson damping function (D3BJ)[44]. Core electrons were replaced by PBE-based projector-augmented-wave potentials[45], whereas we treated explicitly the C (2 s² 2p²), O (2 s² 2p⁴), and H (1 s) valence electrons using wave functions expanded in plane waves with a cutoff energy of 500 eV. Geometries were optimized with a residual forces threshold of 0.01 eV/Å. The gas-phase PTA molecule was calculated at the point using a 17 × 14 × 10 Å³ simulation box, which ensure that repeated image interactions were negligible. The structures to model CNWs were constructed using slabs cut along the (01−10) direction of the DFT-optimized bulk graphite with AA stacking. This cutting direction allowed us to obtain zig-zag terminated edges in the prismatic sites while minimizing the amount of dangling bonds at the surface. The slabs contained three layers of carbon atoms and we fixed the bottom layer to its DFT-optimized position during relaxation procedures. We considered a 20 Å vacuum between slabs. To study the adsorption of PTA on the graphitic surface we used 2 × 2 × 1 k-point meshes and two different supercells (5 × 5 and 7 × 4) as shown in Supplementary Figure 8. For both cases we let the PTA molecules to relax in all three x-, y-, and z-directions as well as a further relaxation of the two top-most carbon layers of the CNW surface model. This setup ensures that absorbed PTA species are separated by at least 9 Å with respect to their neighboring images.

PTA adsorption on the edge surface of graphite. The adsorption energies of PTA molecules on the edge surface of graphite were computed as follow:

$$E_{\text{ads–PTA@C}} = E_{\text{PTA@C}} - E_{\text{C}} - E_{\text{PTA}} \qquad (3)$$

Where $E_{\text{PTA@C}}$, E_{C}, and E_{PTA} are the DFT total energies of the adsorbed PTA molecule, the relaxed bare graphite slab, and the gas-phase PTA molecule,

respectively. The most stable structures and adsorption energies for PTA@C-planar, PTA@C-vertical, and PTA@C-side configurations are shown in Fig. 1. Other less stable structures we found are given in Supplementary Figures 9–11.

References

1. Meek, S. T., Greathouse, J. A. & Allendorf, M. D. Metal-organic frameworks: a rapidly growing class of versatile nanoporous materials. *Adv. Mater.* **23**, 249–267 (2011).
2. Xia, W., Mahmood, A., Zou, R. Q. & Xu, Q. Metal-organic frameworks and their derived nanostructures for electrochemical energy storage and conversion. *Energy Environ. Sci.* **8**, 1837–1866 (2015).
3. Bennett, T. D., Cheetham, A. K., Fuchs, A. H. & Coudert, F. X. Interplay between defects, disorder and flexibility in metal-organic frameworks. *Nat. Chem.* **9**, 11–16 (2016).
4. Furukawa, H., Cordova, K. E., O'Keeffe, M. & Yaghi, O. M. The chemistry and applications of metal-organic frameworks. *Science* **341**, 1230444 (2013).
5. Li, S. L. & Xu, Q. Metal-organic frameworks as platforms for clean energy. *Energy Environ. Sci.* **6**, 1656–1683 (2013).
6. Zhang, J., Hu, H., Li, Z. & Lou, X. W. Double-shelled nanocages with cobalt hydroxide inner shell and layered double hydroxides outer shell as high-efficiency polysulfide mediator for lithium-sulfur batteries. *Angew. Chem. Int. Ed.* **55**, 3982–3986 (2016).
7. Cao, X. H. et al. Metal oxide-coated three-dimensional graphene prepared by the use of metal-organic frameworks as precursors. *Angew. Chem. Int. Ed.* **53**, 1404–1409 (2014).
8. Xia, B. Y. et al. A metal–organic framework-derived bifunctional oxygen electrocatalyst. *Nat. Energy* **1**, 15006 (2016).
9. Aubrey, M. L. & Long, J. R. A dual-ion battery cathode via oxidative insertion of anions in a metal-organic framework. *J. Am. Chem. Soc.* **137**, 13594–13602 (2015).
10. Yang, J., Xiong, P. X., Zheng, C., Qiu, H. Y. & Wei, M. D. Metal-organic frameworks: a new promising class of materials for a high performance supercapacitor electrode. *J. Mater. Chem. A* **2**, 16640–16644 (2014).
11. Yang, J., Zheng, C., Xiong, P. X., Li, Y. F. & Wei, M. D. Zn-doped Ni-MOF material with a high supercapacitive performance. *J. Mater. Chem. A* **2**, 19005–19010 (2014).
12. Liu, X. X. et al. Cobalt-based layered metal-organic framework as an ultrahigh capacity supercapacitor electrode material. *ACS Appl. Mater. Interfaces* **8**, 4585–4591 (2016).
13. Qu, C. et al. Nickel-based pillared MOFs for high-performance supercapacitors: design, synthesis and stability study. *Nano Energy* **26**, 66–73 (2016).
14. Liu, Q. et al. A copper-based layered coordination polymer: synthesis, magnetic properties and electrochemical performance in supercapacitors. *Dalton Trans.* **44**, 19175–19184 (2015).
15. Tan, Y., Zhang, W., Gao, Y., Wu, J. & Tang, B. Facile synthesis and supercapacitive properties of Zr-metal organic frameworks (UiO-66). *RSC Adv.* **5**, 17601–17605 (2015).
16. Du, M. et al. A channel-type mesoporous In(iii)–carboxylate coordination framework with high physicochemical stability for use as an electrode material in supercapacitors. *J. Mater. Chem. A* **2**, 9828–9834 (2014).
17. Zhou, Y., Mao, Z., Wang, W., Yang, Z. & Liu, X. In-situ fabrication of graphene oxide hybrid Ni-based metal–organic framework (Ni–MOFs@GO) with ultrahigh capacitance as electrochemical pseudocapacitor materials. *ACS Appl. Mater. Interfaces* **8**, 28904–28916 (2016).
18. Yoo, J. J. et al. Ultrathin planar graphene supercapacitors. *Nano Lett.* **11**, 1423–1427 (2011).
19. Park, H. J. et al. Layer-by-layer assembled films of perylene diimide- and squaraine-containing metal-organic framework-like materials: solar energy capture and directional energy transfer. *ACS Appl. Mater. Interfaces* **8**, (24983–24988 (2016).
20. So, M. C. et al. Layer-by-layer fabrication of oriented porous thin films based on porphyrin-containing metal-organic frameworks. *J. Am. Chem. Soc.* **135**, 15698–15701 (2013).
21. Shekhah, O. et al. Controlling interpenetration in metal-organic frameworks by liquid-phase epitaxy. *Nat. Mater.* **8**, 481–484 (2009).
22. Dumee, L. et al. Seeded growth of ZIF-8 on the surface of carbon nanotubes towards self-supporting gas separation membranes. *J. Mater. Chem. A* **1**, 9208–9214 (2013).
23. Falcaro, P. et al. Centimetre-scale micropore alignment in oriented polycrystalline metal-organic framework films via heteroepitaxial growth. *Nat. Mater.* **16**, 342–348 (2016).
24. Han, S., Wu, D. Q., Li, S., Zhang, F. & Feng, X. L. Porous graphene materials for advanced electrochemical energy storage and conversion devices. *Adv. Mater.* **26**, 849–864 (2014).
25. Falcaro, P., Buso, D., Hill, A. J. & Doherty, C. M. Patterning techniques for metal organic frameworks. *Adv. Mater.* **24**, 3153–3168 (2012).
26. Furukawa, S., Reboul, J., Diring, S., Sumida, K. & Kitagawa, S. Structuring of metal-organic frameworks at the mesoscopic/macroscopic scale. *Chem. Soc. Rev.* **43**, 5700–5734 (2014).
27. Jahan, M., Bao, Q. L., Yang, J. X. & Loh, K. P. Structure-directing role of graphene in the synthesis of metal-organic framework nanowire. *J. Am. Chem. Soc.* **132**, 14487–14495 (2010).
28. Jahan, M., Liu, Z. L. & Loh, K. P. A graphene oxide and copper-centered metal organic framework composite as a Tri-functional catalyst for HER, OER, and ORR. *Adv. Func. Mater.* **23**, 5363–5372 (2013).
29. Yan, H. et al. Promoted multimetal oxide catalysts for the generation of hydrogen via ammonia decomposition. *J. Phys. Chem. C* **120**, 7685–7696 (2016).
30. Petit, C. & Bandosz, T. J. MOF–graphite oxide composites: combining the uniqueness of graphene layers and metal–organic frameworks. *Adv. Mater.* **21**, 4753–4757 (2009).
31. Miller, J. R., Outlaw, R. A. & Holloway, B. C. Graphene double-layer capacitor with AC line-filtering performance. *Science* **329**, 1637–1639 (2010).
32. Zhao, X. et al. Carbon nanosheets as the electrode material in supercapacitors. *J. Power Sources* **194**, 1208–1212 (2009).
33. Bo, Z. et al. Vertically oriented graphene bridging active-layer/current-collector interface for ultrahigh rate supercapacitors. *Adv. Mater.* **25**, 5799–5806 (2013).
34. Yang, J., Ma, Z., Gao, W. & Wei, M. Layered structural Co-based MOF with conductive network frames as a new supercapacitor electrode. *Chem. Eur. J.* **23**, 631–636 (2017).
35. Sadakiyo, M., Yamada, T. & Kitagawa, H. Rational designs for highly proton-conductive metal-organic frameworks. *J. Am. Chem. Soc.* **131**, 9906–9907 (2009).
36. Talin, A. A. et al. Tunable electrical conductivity in metal-organic framework thin-film devices. *Science* **343**, 66–69 (2014).
37. Liu, C., Li, F., Ma, L. P. & Cheng, H. M. Advanced materials for energy storage. *Adv. Mater.* **22**, E28–E62 (2010).
38. Zhao, X., Sanchez, B. M., Dobson, P. J. & Grant, P. S. The role of nanomaterials in redox-based supercapacitors for next generation energy storage devices. *Nanoscale* **3**, 839–855 (2011).
39. Kresse, G. & Hafner, J. Ab initio molecular dynamics for liquid metals. *J. Phys. Rev. B* **47**, 558–561 (1993).
40. Kresse, G. & Furthmüller, J. Efficiency of ab-initio total energy calculations for metals and semiconductors using a plane-wave basis set. *Comput. Mater. Sci.* **6**, 15–50 (1996).
41. Kresse, G. & Furthmüller, F. Efficient iterative schemes for ab initio total-energy calculations using a plane-wave basis set. *Phys. Rev. B* **54**, 11169–11186 (1996).
42. Perdew, J. P., Burke, K. & Ernzerhof, M. Generalized gradient approximation made simple. *Phys. Rev. Lett.* **77**, 3865–3868 (1996).
43. Grimme, S., Antony, J., Ehrlich, S. & Krieg, H. A. A consistent and accurate ab initio parametrization of density functional dispersion correction (DFT-D) for the 94 elements H-Pu. *J. Chem. Phys.* **132**, 154104 (2010).
44. Grimme, S., Ehrlich, S. & Goerigk, L. Effect of the damping function in dispersion corrected density functional theory. *J. Comput. Chem.* **32**, 1456–1465 (2011).
45. Kresse, G. & Joubert, D. From ultrasoft pseudopotentials to the projector augmented-wave method. *Phys. Rev. B* **59**, 1758–1775 (1999).

Acknowledgements

Author contributions

W.Z., W.T.Z. and T.D. conceived and coordinated the study and led writing of the manuscript. T.D. conducted all the experiments. O.A. and J.C. contributed the theoretical calculations and analysis. All co-authors commented on the manuscript.

Additional information

Supplementary information is available for this paper at https://doi.org/10.1038/s42004-017-0005-8.

Competing interests: The authors declare no competing financial interests.

Reprints and permission information is available online at http://npg.nature.com/reprintsandpermissions/

Publisher's note: Springer Nature remains neutral with regard to jurisdictional claims in published maps and institutional affiliations.